

Rapid breakdown anodization technique for the synthesis of high aspect ratio and high surface area anatase TiO_2 nanotube powders

Rajini P. Antony ^a, Tom Mathews ^{a,*}, Arup Dasgupta ^b, S. Dash ^a, A.K. Tyagi ^a, Baldev Raj ^{a,b}

^a Thin Films and Coatings Section, Surface and Nanoscience Division, Materials Science Group, Indira Gandhi Centre for Atomic Research, Kalpakkam 603102, Tamil Nadu, India

^b Physical Metallurgy Division, Indira Gandhi Centre for Atomic Research, Kalpakkam 603102, Tamil Nadu, India

ARTICLE INFO

Article history:

Received 11 October 2010

Received in revised form

22 December 2010

Accepted 17 January 2011

Available online 25 January 2011

Keywords:

Rapid breakdown anodization

Titania nanotubes

Band gap

ABSTRACT

Clusters of high aspect ratio, high surface area anatase- TiO_2 nanotubes with a typical nanotube outer diameter of about 18 nm, wall thickness of approximately 5 nm and length of 5–10 μm were synthesized, in powder form, by breakdown anodization of Ti foils in 0.1 M perchloric acid, at 10 V (299 K) and 20 V (~275 and 299 K). The surface area, morphology, structure and band gap were determined from Brunauer Emmet Teller method, field emission scanning electron microscopy, transmission electron microscopy, X-ray diffraction, Raman, photoluminescence and diffuse reflectance spectroscopic studies. The tubular morphology and anatase phase were found to be stable up to 773 K and above 773 K anatase phase gradually transformed to rutile phase with disintegration of tubular morphology. At 973 K, complete transformation to rutile phase and disintegration of tubular morphology were observed. The band gap of the as prepared and the annealed samples varied from 3.07 to 2.95 eV with increase in annealing temperature as inferred from photoluminescence and diffuse reflectance studies.

© 2011 Elsevier Inc. All rights reserved.

1. Introduction

From the fundamental and applied perspective nanostructured TiO_2 has been attracting particular attention because of its tailored geometry yielding desirable properties which can be made use of in the field of water photoelectrolysis, photocatalysis, self-cleaning devices, solar energy conversion, gas sensor and hydrogen storage[1–7]. Since the material is very important in the field of nanotechnology for making functional devices for various purposes, production of highly efficient nanostructures in a cheap, tuneable and easily controllable manner, is of high scientific and technological interest. Classical methods to produce nanoporous and nanoparticulates of TiO_2 include sol-gel and hydrothermal synthesis. For applications in devices such as solar cells where enhanced electron transfer and efficient light to electrical energy conversion are needed one dimensional TiO_2 nanostructures such as nanotubes, nanowires and nanobelts are more efficient compared to nanoparticulates. TiO_2 nanotubes of different sizes were synthesized by various research groups adopting hydrothermal, sol-gel and template based synthesis techniques [8–10]. With the successful electrochemical synthesis of TiO_2 nanotubes on Ti foil by Zwilling et al. [11] in 1999, the

anodization process for developing TiO_2 nanotubes became exciting. Following this method, TiO_2 nanotube arrays were synthesized in HF based acidic electrolytes by Beranek et al. in 2003 [12]. However, the lengths of the nanotubes were limited to 500 nm. This limitation was attributed to the chemical dissolution of Ti as well as TiO_2 into the electrolytic solution. Later several groups studied these limitations and successfully synthesized nanotube arrays of lengths up to several microns by varying the pH of the solution by adding NH_4F , NaF and KF instead of HF [13–16]. Paulose et al. [17] synthesized TiO_2 nanotube arrays of lengths up to thousand micrometers on titanium foils. This length was achieved by using non-aqueous organic electrolytes such as glycerol, ethylene glycol, DMSO and Formamide [18,19]. Various research groups analyzed change in morphological parameters like aspect ratio, wall thickness, pore size and roughness by varying the electrochemical parameters such as applied potential, electrolyte concentration, anodization duration, temperature and pH of the electrolyte solution [20–23]. Simultaneously researches were carried out to understand the mechanism of nanotube formation during anodization [24,25]. From their results it was commonly accepted that field assisted chemical oxidation of Ti to TiO_2 , field assisted chemical dissolution of Ti and TiO_2 as $[\text{TiF}_6]^{2-}$ and the localized chemical etching of TiO_2 surface by F^- ions are the main processes taking place during the nanotube formation. Even though the anodization of Ti foil in fluoride ion containing medium resulted in self-organized TiO_2

* Corresponding author.

E-mail address: tom@igcar.gov.in (T. Mathews).

nanotube arrays, these possessed certain limitations in specific applications such as dye sensitized solar cells and photocatalytic reactions because the nanotube arrays when used in the above mentioned applications requires back side illumination which reduces light to electrical energy conversion efficiency. In addition, the Ti metal substrates on which the TiO_2 nanotubes are formed causes short circuits in devices. Therefore, further researches were carried out to develop TiO_2 nanotube arrays by anodizing Ti thin films deposited on various substrates such as glass, quartz, silicon and conducting glasses [26–28]. In this case, the quality of the film is of utmost importance. When the adherences of the films were poor, the rate of chemical dissolution was high which prevented the nanotube formation. By optimizing the thin film deposition and anodization parameters Oomen et al. synthesized nanotubes of few micrometers length on quartz and glass substrates [29].

In all the above-mentioned cases, the syntheses of TiO_2 nanotube arrays were done in fluoride ion containing electrolytic medium. From these studies, it was hypothesized that fluoride ions play a major role in the formation of nanotube, since it has the ability to dissolve Ti and TiO_2 as $[\text{TiF}_6]^{2-}$ complex. Extending this hypothesis to chloride ion containing medium, Hahn et al. [30] synthesized nanotubes of TiO_2 and WO_3 in sodium per chlorate and perchloric acid media. Later several research groups successfully synthesized TiO_2 nanotube arrays by anodizing Ti foil in chloride ion containing aqueous electrolytes [31–34].

To overcome the limitations of TiO_2 nanotube arrays on Ti foils in device applications efforts were also directed towards synthesis of TiO_2 nanotubes in powder form, which can be used for coating on desired substrates by spray coating, spin coating, dip coating and screen-printing. In 2009 Fahim and Sekino synthesized nanotubes of TiO_2 in powder form by electrochemical anodization technique using Ti foils in perchloric acid and sodium chloride/sodium phosphate media and the electrochemical approach was termed as rapid breakdown anodization technique [35]. They obtained TiO_2 nanotube powders, which were X-ray amorphous, and upon heating crystallized to anatase phase in the temperature range 573–773 K. Heating beyond 773 K caused anatase to rutile phase transformation.

Following the method prescribed by Fahim and Sekino, the present study describes the synthesis of ultrahigh surface area TiO_2 nanotube powders having wall thickness, pore diameter as well as particle size less than those reported by Fahim and Sekino. In the present study anatase- TiO_2 nanotube powders were obtained in the as prepared state itself. Anodization was carried out at 20 and 10 V in perchloric acid medium at room temperature. One low temperature (275 K) synthesis was also carried out at 20 V to study the effect of temperature. Structure, morphology and optical properties of the as prepared and annealed samples as well as the annealing temperature limit for maintaining the tubular morphology and phase purity were investigated.

2. Experimental details

2.1. Synthesis of titania nanotube powders

Titanium foils of 0.5 mm thickness (99% purity, Alfa aesar) and Pt foils were chosen for the anodization process. The foils were cut into 10 mm × 10 mm pieces and degreased by sonicating in deionized water, ethanol, isopropyl alcohol and then in acetone. The cleaned foils were then dried in nitrogen stream. Reagent grade perchloric acid was chosen as the electrolyte.

The titanium foils and the platinum cathode were connected to electrical leads by means of crocodile clips and dipped into the electrolyte solution (0.1 M perchloric acid). The distance between the electrodes was maintained at 15 mm. Two anodization

experiments, one at room temperature (10 and 20 V) and the other at ~275 K (20 V) were carried out. The variation of current with time, during anodization, were recorded using a computer controlled digital multimeter (HP 34401A). Anodization was continued until the Ti foil completely transformed into TiO_2 powder. The white powders obtained after anodization at 10 V (299 K), 20 V (299 K) and 20 V (275 K) were named as NP1, NP2 and NP3, respectively. These powders were washed several times with deionised water, centrifuged and dried overnight at 323 K in a Petri dish. The samples were then annealed at 673, 773, 873 and 973 K, at a heating rate of 3° per minute, for 2 h and then cooled slowly. The as prepared and annealed samples were then characterized using various techniques.

2.2. Characterization

The surface area of the samples were measured by Brunauer Emmet Teller (BET) adsorption method (Sorptomatic 1990, Thermo Electron Corporation, USA). Nitrogen gas was used as the adsorbate. The microscopic analyses of the samples were done by field emission scanning electron microscope (FESEM) (FEG Quanta, Philips, Netherlands) and transmission electron microscope (TEM) (Philips, Netherlands). The scanning electron micrographs of the gold sputtered TiO_2 powder samples were taken by applying 15 kV accelerating voltage keeping a working distance of 6.4 cm. The composition of the samples were analyzed by energy dispersive X-ray analyzer (EDAX). The samples for TEM studies were prepared by placing a drop of methanol, in which the powder was dispersed by sonication, on carbon coated copper grid and allowing it to dry. The crystal structure of the nanotube powders were analyzed by selected area electron diffraction (SAED). X-ray diffraction studies were also done to identify the crystalline phases of the as prepared and annealed samples using a STO1 X-ray diffractometer (Germany). Diffraction studies were carried out using $\text{CuK}\alpha$ ($\lambda=1.54060\text{ \AA}$) radiation at 40 kV and 30 mA with a scan step of 1° over 20–70°. The XRD pattern of the samples were compared with the JCPDS file 21-1272 and 21-1276 corresponding to anatase and rutile phases, respectively. The crystallite sizes of the as prepared samples were calculated using Scherer formula [36]:

$$t = K\lambda/B\cos\theta$$

where K is a dimensionless constant having value 0.9, $\lambda=1.5406\text{ \AA}$ and θ is the diffraction angle in radians. Broadening B was calculated by taking the full width half maximum of the diffraction peak corresponding to each plane in the diffraction pattern. Raman scattering measurements were carried out for the as prepared samples using the 532 nm line of a diode-pumped solid state laser as the excitation and analyzed using a double-monochromator (Jobin-Y von U1000), equipped with a liquid nitrogen cooled charge-coupled device (CCD) detector. The photoluminescence (PL) measurements were carried out using the Jobin Yvon-Spex make Spectrofluorometer (Fluorolog version-3; Model FL3-11) with 450 W high-pressure xenon arc lamp as excitation source. PL excitation and emission spectra were acquired at room temperature for a spectral resolution of 0.2 nm and slit width of 0.25 mm. Further optical characterization of the samples was done by UV-vis diffuse reflectance spectrophotometer (Shimadzu UV 2401). The reflectance spectra were taken over the range 800–200 nm at a scan rate of 100 nm/s. BaSO_4 was used as the reference.

3. Results and discussions

3.1. Potentiostatic transient behavior

The variation of current with time during the electrochemical processes is shown in Fig. 1. During initial stages of anodization,

formation of a white layer of titanium dioxide was observed on the surface of the Ti metal, which started breaking down into the electrolytic solution as white powders. The anodization reaction can be represented as



The rate of oxide formation is faster in the initial stage and a white TiO_2 layer is formed on the metal surface. After that, the TiO_2 starts dissolving because of electrochemical etching by chloride ions giving rise to the formation of pits, and consequent inward migration of oxide ions results in the formation of a thick layer of TiO_2 and reduction in current. In addition, the chloride ions etched the Ti metal leading to the dissolution of Ti as $[\text{TiCl}_6]^{2-}$. The electrochemical etching of Ti metal facilitated the easy breakdown of the oxide layer. Because of the high mechanical stress between the metal and metal oxide interface, a small disturbance is capable of causing removal of the metal oxide layer from the metal surface. This disturbance was provided by chemical reactions in the electrolyte, strong bubbling in the solution due to hydrogen evolution at the cathode as well as stirring. The periodic release of oxide layer continued until complete conversion of Ti metal to TiO_2 . The current–time profile of the room temperature anodization performed at 10 and 20 V (Fig. 1) are similar except for the current magnitude and time duration for each stage. The differences can be

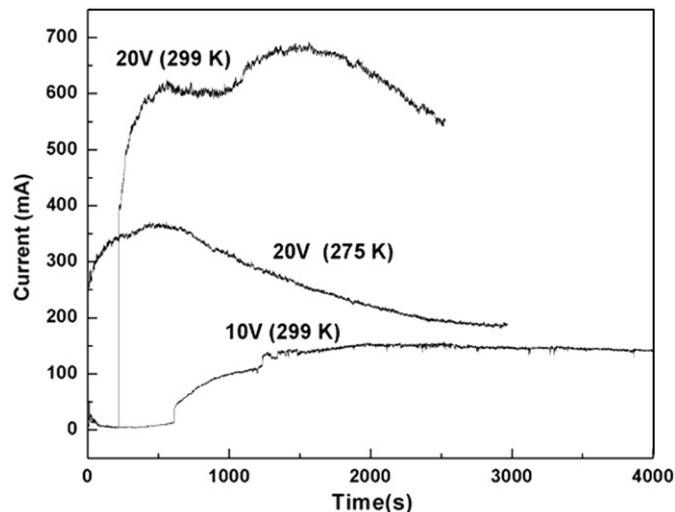


Fig. 1. Variation of current with time during anodization.

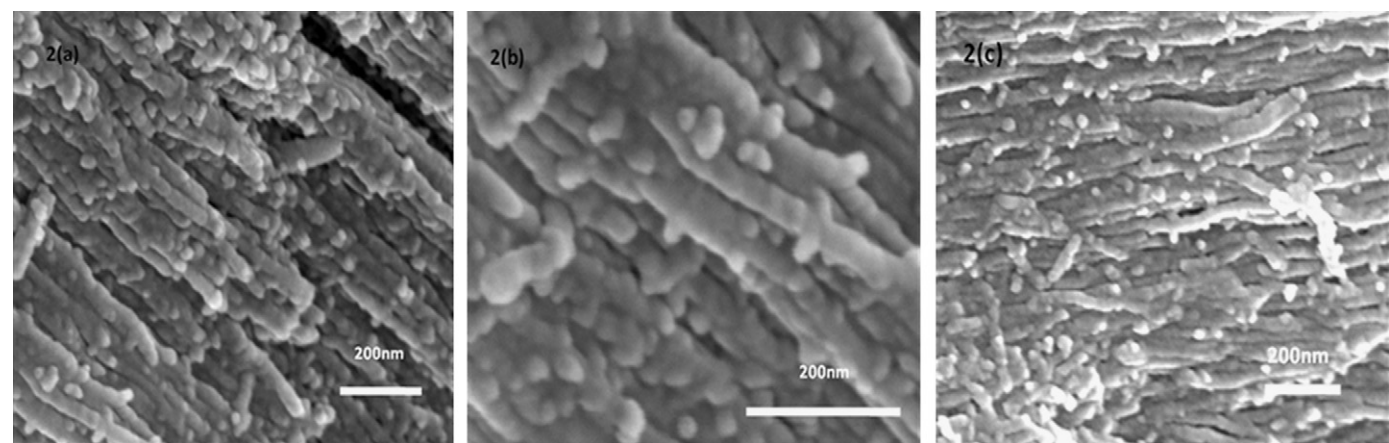


Fig. 2. FESEM images of the TiO_2 nanotube powders synthesized at different conditions: (a) 10 V and ~ 299 K (NP1), (b) 20 V and ~ 299 K (NP2), and (c) 20 V ~ 225 K (NP3).

attributed to the change in kinetics with applied potential. During room temperature anodization at 20 V the electrolyte bath temperature increased by $\sim 15\text{--}18$ °C whereas, the rise in temperature was only ~ 3 °C at 10 V. The relatively large rise in temperature, at 20 V, led to large increase in current. In addition, the breakdown of titanium oxide layer started within minutes of anodization at 20 V exposing fresh metal surface whereas, the onset as well as rate of oxide layer breakdown was slow at 10 V. In the case where applied voltage and electrolyte temperature were 20 V and ~ 275 K, the current increased slowly and then decreased very slowly until the Ti metal was oxidized completely to TiO_2 . The slow change in current with time is because of the slow reaction kinetics at low temperature.

3.2. Surface area measurements

The surface area of the sample NP1 calculated from BET adsorption plot is 155 g/m^2 . The high specific surface area of the nanotube powders point towards the availability of large number of catalytic sites on the nanotube walls. The material is a promising candidate for sensor applications because of high specific surface area.

3.3. Field emission scanning electron microscopic studies

The FESEM images of the TiO_2 powder samples NP1, NP2 and NP3 are shown in Figs. 2a–c, respectively. SEM images of these powders reveal clusters of nanotubes of high aspect ratio. The SEM images indicate that changes in the experimental conditions did not change the morphology but the growth rate. The growth rate decreased with decrease in temperature as well as applied potential. The outer diameter of the nanotube was about 18 nm and the length was approximately 5–10 μm . Though the tube walls appear smooth with nanoparticles sitting on it, a close observation of the micrograph reveal that the walls consist of nanograins. The diameter of the tube increases in the order NP1 (10 V, 299 K) $<$ NP3 (20 V, 275 K) $<$ NP2 (20 V, 299 K).

Figs. 3 and 4 show the FESEM images of the nanotube powders annealed at different temperatures. An increase in particulate like morphology is seen on annealing and the particle size increases with increase in annealing temperature. The nanograins/nanoparticles that constitute the nanotube walls became more visible on annealing. The SEM images of the samples (NP1) annealed at 673 and 773 K reveals that the overall morphology of the samples is retained, although the nanograins which constitute the tube walls are clearly visible (Figs. 3a and b). The SEM image of the samples

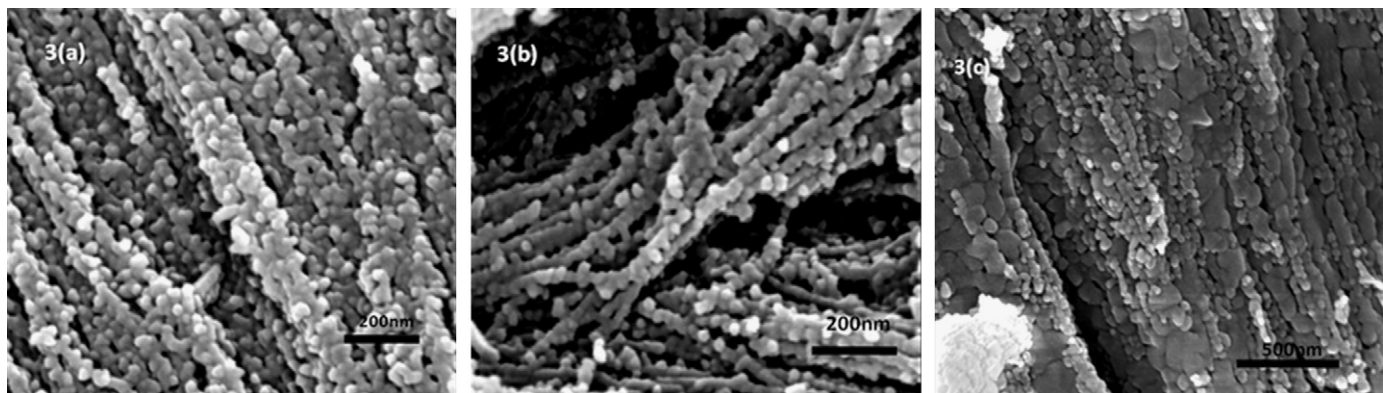


Fig. 3. FESEM images of NP1 samples annealed at different temperatures: (a) 673 K, (b) 773 K and (c) 873 K.

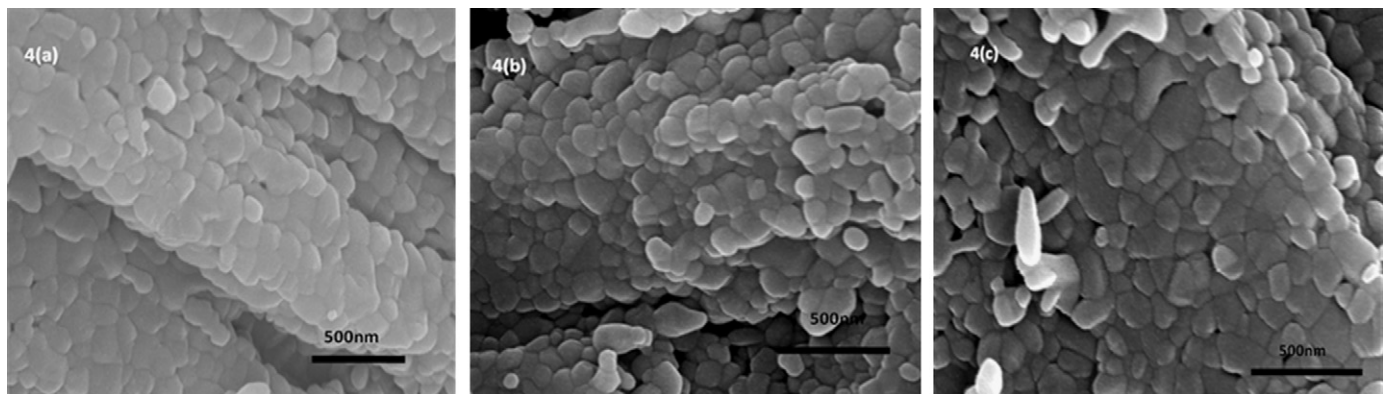


Fig. 4. (a)–(c) FESEM images of NP1, NP2 and NP3 samples annealed at 973 K.

(NP1) annealed at 873 K shows that the nanotubes start to disintegrate to particles resulting in a morphology having both nanotubes and nanoparticles (Fig. 3c). Similar features are seen in the case of NP2 and NP3 samples annealed at 673, 773 and 873 K. Fig. 4 depicts the SEM images of the samples (NP1, NP2, and NP3) annealed at 973 K. An increase in disintegration of tubular morphology in the order $NP1 < NP2 \leq NP3$ can be discerned.

3.4. Transmission electron microscopic studies

The TEM image of the as prepared sample (NP1) revealing the tubular microstructure of the powders is shown in Fig. 5. The tubes are of uniform width measuring about 15–18 nm in diameter. The inner diameter of the tubes varies from 5 to 8 nm and the wall thickness is about 5 nm. Similar images were obtained for NP2 and NP3 samples. Fig. 6 shows the SAED pattern of sample NP1, the different (*hkl*) planes were identified as (101), (103), (105), (204) and (116) of anatase phase. TEM studies were also carried out for the annealed samples of nanotube powders synthesized at 10 V (NP1). The sample annealed at 873 K (Fig. 7a) shows a mixture of tubular and particle morphology. At 973 K the tubular morphology is completely lost resulting in the formation of particles as shown in Fig. 7b. The results obtained from the TEM results are in agreement with the SEM observations. The SAED pattern (Fig. 8) of the sample annealed at 973 K reveals that the sample is of rutile phase in agreement with the XRD results.

3.5. Powder X-ray diffraction studies

The crystalline nature of the as prepared samples is further confirmed by XRD. Fig. 9 depict the XRD pattern of the as prepared samples. The pattern matches well with that of anatase

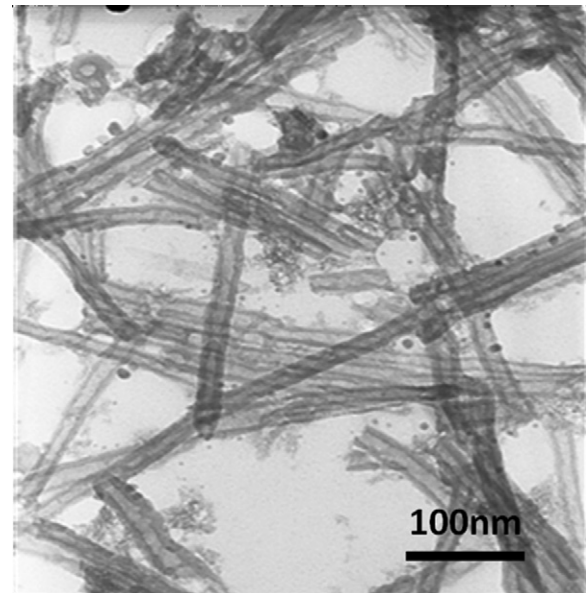


Fig. 5. TEM image of the TiO_2 nanotube powders synthesized at 10 V (~ 26 °C).

phase. The presence of broad peaks indicates that the crystallite size is in the nanometer regime. The crystallite size calculated for the samples NP1, NP2 and NP3, using Scherer formula, are 10, 13 and 12 nm, respectively. The electrochemical synthesis of anatase phase of nanotube powders without any post annealing is reported for the first time. The XRD patterns of the as prepared and annealed NP1 samples are shown in Fig. 10. From the XRD

patterns, it is clear that the anatase phase is stable up to 773 K. XRD pattern of the sample annealed at 873 K shows the presence of both rutile and anatase phases. At 973 K complete transformation to rutile phase has taken place. **Fig. 11** shows the variation of crystallite size with temperature. The curve represents a linear change in crystallite size until a temperature of 773 K. Beyond this the crystallite size ballistically shoots up. It is evident from the FESEM, TEM and XRD results that the tubular morphology and anatase phase are stable only up to a temperature of 773 K. These results indicate that from application point of view where the anatase-TiO₂ nanotubes are more efficient, the sample should preferably be annealed below 773 K.

3.6. Raman spectroscopy analysis

The crystal structure of anatase-TiO₂ is tetragonal (space group D_{4h}^{19} ($I4_1/AMD$)) with two TiO₂ units in the primitive cell giving

six Raman active phonons in the vibrational spectra: three E_g (144, 197 and 639 cm⁻¹), two B_{1g} (399 and 519 cm⁻¹) and one A_{1g} (513 cm⁻¹) [37]. Raman spectra show broadening and shifting of bands with decrease in particle size/size confinement in one or more dimension. However, the effect of phonon confinement is examined based on shape and position of the intense E_g mode appearing at 144 cm⁻¹. **Fig. 12** shows the Raman spectra of the as prepared TiO₂ nanotube powders. Four peaks appear at around 149, 396, 517 and 638 cm⁻¹ and these peaks are assigned to E_g, B_{1g}, B_{1g}/A_{1g} and E_g modes, respectively. The intense low frequency band at 149 cm⁻¹ is because of the O-Ti-O bending vibrations and is a characteristic feature of anatase phase. All the four peaks correspond to the Raman active phonon modes of tetragonal anatase phase of TiO₂ [37]. It can be seen that the intense Raman peak corresponding to the E_g mode of TiO₂ (144 cm⁻¹ for standard bulk samples) has shifted towards higher wave

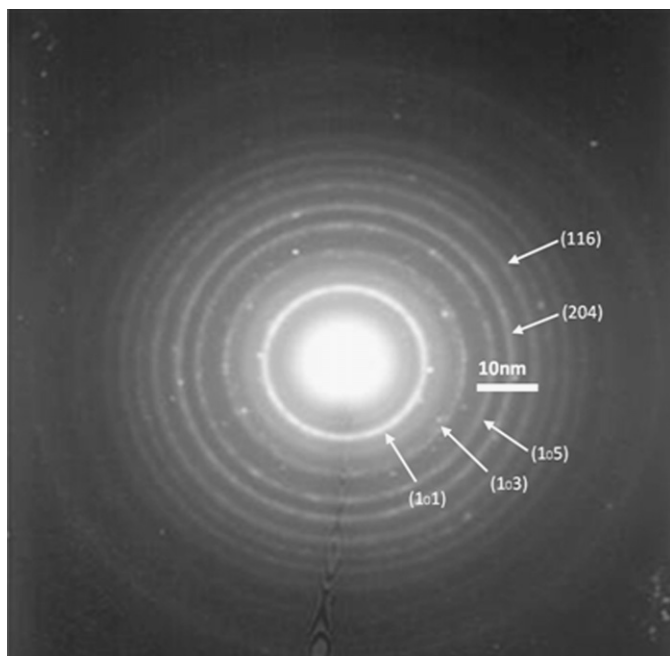


Fig. 6. SAED pattern of NP1 (as prepared).

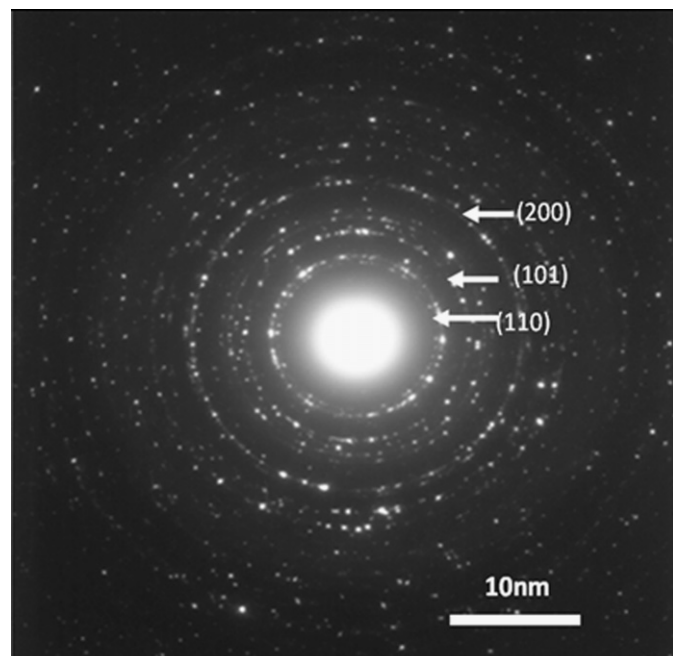


Fig. 8. SAED pattern of the NP1 annealed at 973 K.

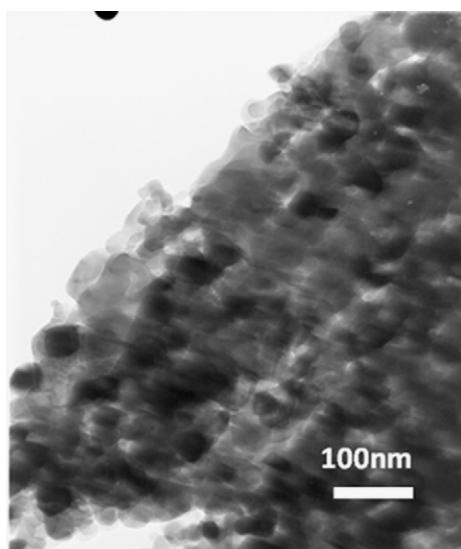
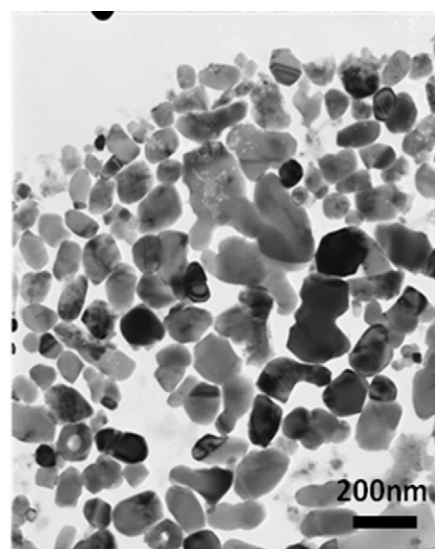


Fig. 7. TEM images (a) NP1 annealed at 873 K and (b) NP1 annealed at 973 K (shows complete destruction of tubular morphology).



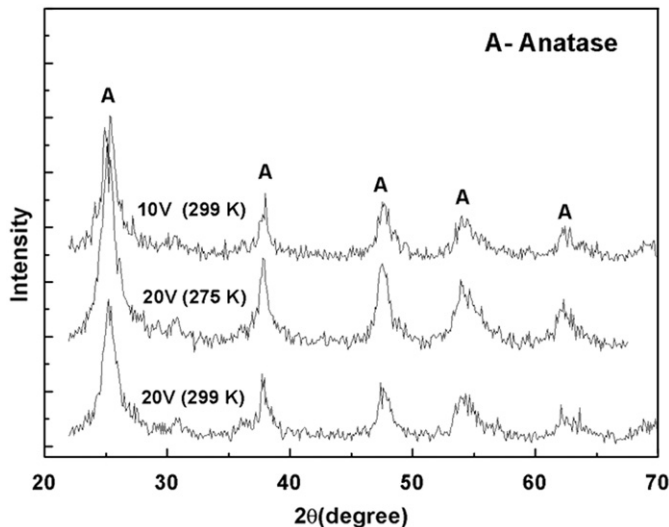


Fig. 9. XRD pattern of the as prepared samples (NP1, NP2 and NP3).

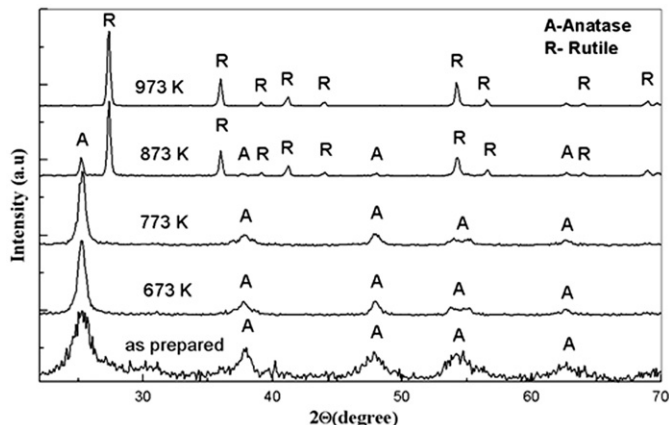


Fig. 10. XRD patterns of NP1 samples (as prepared and annealed at various temperatures).

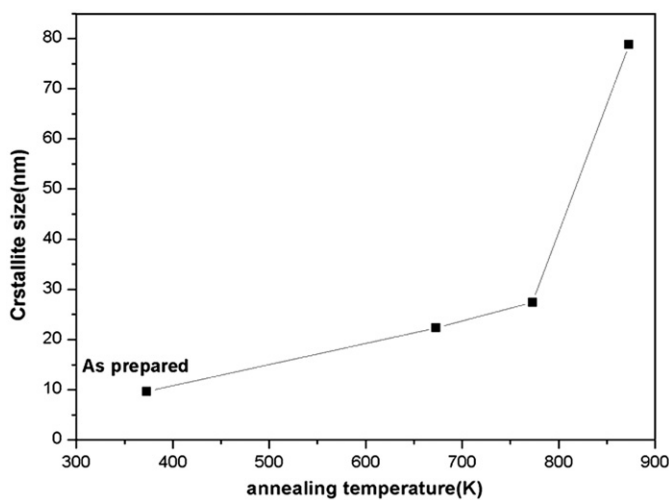


Fig. 11. Variation of crystallite size, of the NP1 samples, with temperature.

number and the FWHM is high compared to those of standard microcrystalline samples. The shift and broadening of the Raman peaks observed in this study suggest the presence of size effects

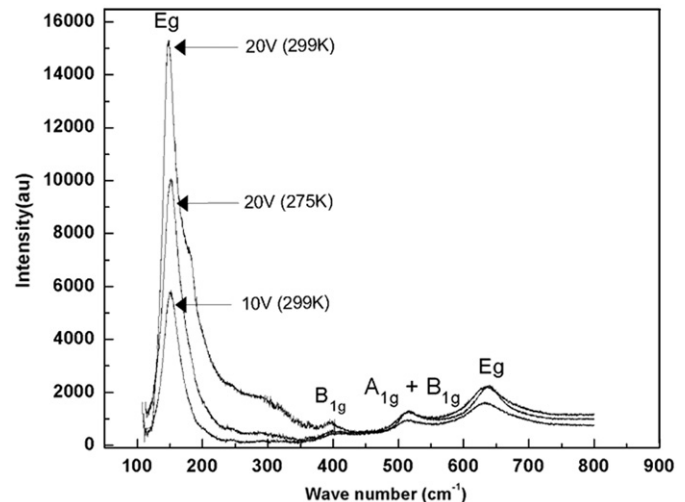


Fig. 12. Raman spectra of the as prepared samples (NP1, NP2 and NP3).

and can be attributed to the quantum confinement effect in agreement with the literature where quantum confinement effect in TiO_2 nanoparticles giving rise to blue shift is reported [38,39]. The peak positions and FWHM of the Raman peaks of the as prepared samples (NP1, NP2 and NP3), obtained by fitting to Lorenzian, are shown in Table 1. In addition to the shift and broadening an asymmetry is seen on the peak (149 cm^{-1}) which can be attributed to the contribution from the less intense Raman peak at 197 cm^{-1} (E_g). No other peaks corresponding to rutile or any other TiO_2 polymorphs are seen in the spectra, which is in good agreement with XRD results. The detailed Raman study of TiO_2 nanotube powders are in progress.

3.7. Photoluminescence studies

The photoluminescence spectrum is useful to reveal the efficiency of charge carrier trapping and transfer in the case of semiconductors [40]. Fig. 13 shows the PL spectra of the as prepared and annealed NP1 samples. Broad, asymmetric PL bands, tailing towards low photon energies and peaking around 3.1 and 3.0 eV are observed for NP1 as well as NP1 annealed at 673 and 773 K and for NP1 annealed at 873 and 973 K, respectively. The band gaps of the samples evaluated from the peak positions of the PL spectra fitted to Gaussian are 3.12, 3.13, 3.13, 3.02, and 3.01 for NP1, NP1 annealed at 673, 773, 873 and 973 K, respectively. The spectra on deconvolution revealed the presence of three main PL bands. The bands around 3.1 eV (in the case of NP1, NP1 annealed at 673 and 773 K) and 3.0 eV (NP1 annealed at 873 and 973 K) is attributed to the indirect transition. The valence band and conduction band of TiO_2 comprises of $\text{O}-2p$ and $\text{Ti}-3d$ electrons, respectively. For TiO_2 nanotubes, because of high surface to volume ratio, substantial numbers of Ti ions are exposed at the surface. As evident from FTIR studies sufficient numbers of them exist as $\text{O}-\text{Ti}-\text{OH}$. The presence of $\text{Ti}-\text{OH}$ bonds distort the TiO_6 octahedra and introduce localized energy states within the band gap. These charge-carriers trapping surface states with different energy levels become luminescent centers. The PL bands observed around 2.85 eV and the flat bands around 2.65 eV (440–480 nm) with several sharp peaks can be ascribed to luminescence from these surface states that are present on the distorted TiO_6 octahedra (excitons trapped at shallow-trap and medium-trap surface states). It is seen from the spectra that the PL intensity increases as the sample is annealed at 673 K and then starts

Table 1

The wave number and the FWHM (in parentheses) of Raman spectra of the samples.

Sample	E_g	B_{1g}	$A_{1g}+B_{1g}$	E_g
10 V (299 K)/NP1	153.05(30.59)	401.83(40.06)	514.51(86.18)	639.68(111.59)
20 V (299 K)/NP2	149.11(23.04)	398.95(31.23)	516.13(10.59)	639.49(76.04)
20 V (275 K)/NP3	153.12(38.97)	401.74(40.98)	516.62(38.97)	639.34(52.32)

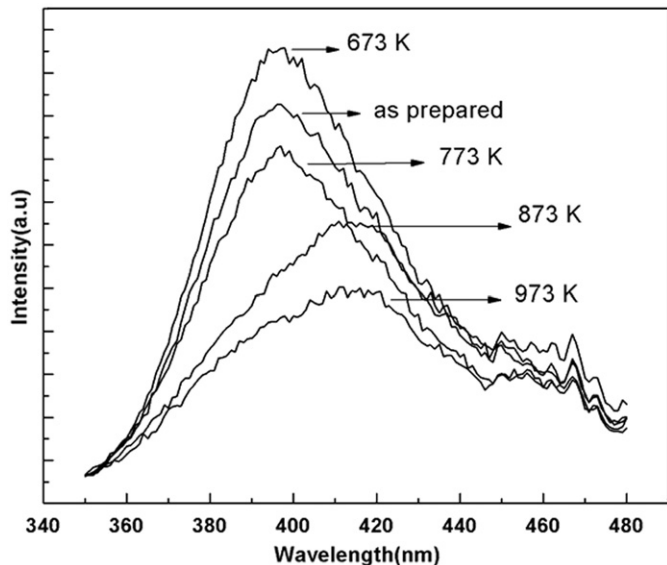


Fig. 13. Photoluminescence spectra of the annealed samples of NP1.

decreasing on annealing at 773 K. The temperature dependence of the PL data may be attributed to the different structural phases and microstructures of the annealed samples. The rise in PL intensity (at 673 K) can be attributed to annealing of defects present in the as prepared sample. The rise in intensity is also accompanied with the reduction in the FWHM signifying reduction in disorder. Further increase in temperature to 773 K causes reduction in spectral intensity. The PL spectra of the as prepared and annealed samples (673 and 773 K) are very similar except for the small difference in intensity. Whereas the spectra of the samples annealed at 873 and 973 K are different and are accompanied with enhanced broadening, decrease in spectral symmetry and intensity. This is because the as prepared and 673 and 773 K annealed samples are of anatase phase whereas the 873 K annealed sample is a mixture of anatase and rutile phases and the sample annealed at 973 K is completely rutile. The presence of rutile phase enhances the broadening and reduces the PL intensity because of its poorer photo-reactivity compared to anatase. The observed gradual red shift indicates anatase to rutile phase transformation in agreement with the XRD and SAED results. The red shift observed in the case of NP1 annealed at 873 K (mixture of rutile and anatase) is induced by charge transfer from anatase to rutile. As the conduction band energy level of anatase is higher than that of rutile some electrons in the anatase particles that are excited from the valence band to the conduction band transfer to the conduction band of rutile, and the photo-induced electrons and holes recombine to give luminescence.

3.8. Optical absorption studies

The absorption studies were carried out by taking the diffuse reflectance spectra (DRS) of the powder samples. There are different methods for determining the band gap (E_g) using

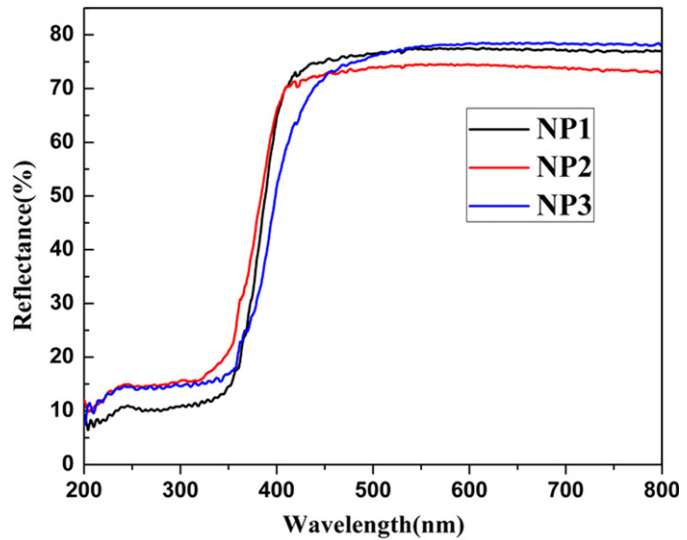


Fig. 14. Diffuse reflectance spectra of the as prepared samples (NP1, NP2 and NP3).

DRS [41–43]. In this work the E_g of the as prepared as well as the annealed TiO_2 nanotubes were determined from the intersection point between energy axis ($h\nu$) and the line extrapolated from the linear portion of the absorption edge of the so called Kubelka–Munk function (re-emission function)

$$KM = \frac{[1-R]^2}{2R} = \frac{\alpha}{S} \quad (2)$$

KM is the Kubelka–Munk function, R the ratio of the intensities of radiation reflected in diffuse manner from the sample and from the known sample, α represents the absorption coefficient of radiation and S is the scattering factor. For very small particles S is approximately unity or it is a constant when the thickness of the sample is much bigger than the individual particle. Therefore, the KM function will be almost equal to the absorption coefficient. For different transition mechanism it has been proved that along the sharp absorption edge, the energy of incident photons and E_g of a semiconductor will have the relation

$$\propto^n = A(h\nu - E_g) \quad (3)$$

or

$$(\propto h\nu)^s = A(h\nu - E_g) \quad (4)$$

where the value 's' depends on the interband transition mechanism. For indirect band gap material s is 0.5, ν is the frequency and h is Plank's constant [44]. Since the re-emission function is equal to the absorption coefficient according to Eq. (1), the Tauc plot, $(\sqrt{\alpha}h\nu)$ versus $h\nu$ can be replaced by $(\sqrt{KB^*h\nu})$ versus $h\nu$. The optical band gap, obtained by extending the line, from the slope of the linear part of the curve, to $x=0$, is 3.07, 3.05 and 2.95 eV for NP1, NP2 and NP3, respectively. Whereas the band gap reported for anatase TiO_2 is 3.4 eV. The reflectance and Tauc plot of the as prepared samples are depicted in Figs. 14 and 15, respectively. Similar plots were obtained for NP1 samples annealed at different temperatures and the band

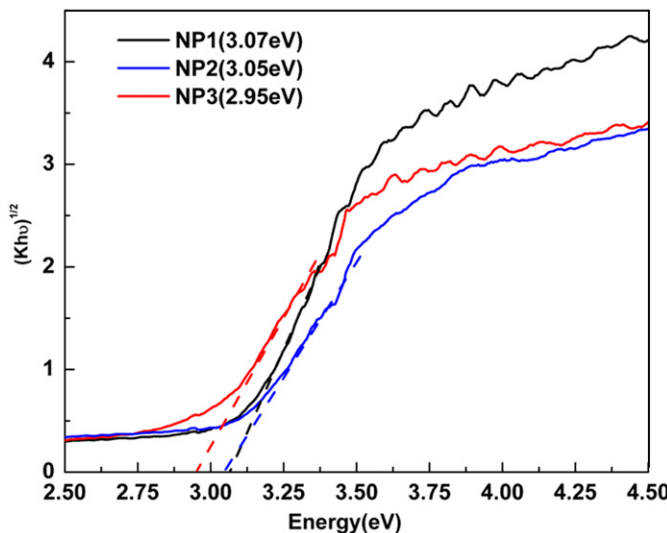


Fig. 15. Tauc plot of the as prepared samples (NP1, NP2 and NP3). The band gap are 3.07, 3.05 and 2.95 for NP1, NP2 and NP3 samples, respectively.

Table 2

Band gap of the TiO_2 nanotubes obtained from photoluminescent and diffuse reflectance studies.

Sample details	Band gap (E_g) calculated from PL (eV)	Band gap (E_g) calculated from DRS (eV)
NP1	3.12	3.07
NP2	–	3.05
NP3	–	2.95
Annealed NP1 (673 K)	3.13	2.85
Annealed NP1 (773 K)	3.13	2.91
Annealed NP1 (873 K)	3.02	2.87
Annealed NP1 (973 K)	3.01	2.88

gap values evaluated from the plots are given in Table 2. In the case of NP1 samples annealed at different temperatures, there is trend of decrease in band gap with increase in annealing temperature. This reflects anatase to rutile phase transformation. The lower band gap of the rutile phase makes the absorption edge around visible region. The decrease in band gap values of the nanotubes compared to those reported can be attributed to the presence of oxygen vacancies created by the chemisorbed hydroxyl groups. As inferred from the FTIR analysis the presence of hydroxyl group on the surface of TiO_2 nanotubes create oxygen vacancies and aggregation of the vacancies lead to decrease in band to band transition energy. The broad peak in the PL spectra also gives evidence of oxygen vacancies, which creates a decrease in the band to band transition energy. Band gaps obtained from both PL and DRS studies are tabulated in Table 2. The mechanism of absorption of light in semiconductor materials involves the use of photon energy to excite the electrons from valence band to the conduction band. In the present case, the absorption is in the visible range close to UV. Therefore, TiO_2 nanotubes could find active use in photovoltaic and photo catalytic applications. The material can be made to absorb in the visible region by appropriate doping which further reduces the band gap. From the density of state calculations Asahi et al. have shown that the band gap of TiO_2 can be engineered to absorb in the visible region by N doping at low concentrations [45]. Reports are also there where N, C and Bi are doped in TiO_2 and decrease in band gap were observed [46,47]. If synthesis and doping can be done simultaneously by rapid breakdown anodization it will be a highly efficient method for the synthesis of visible light active TiO_2 .

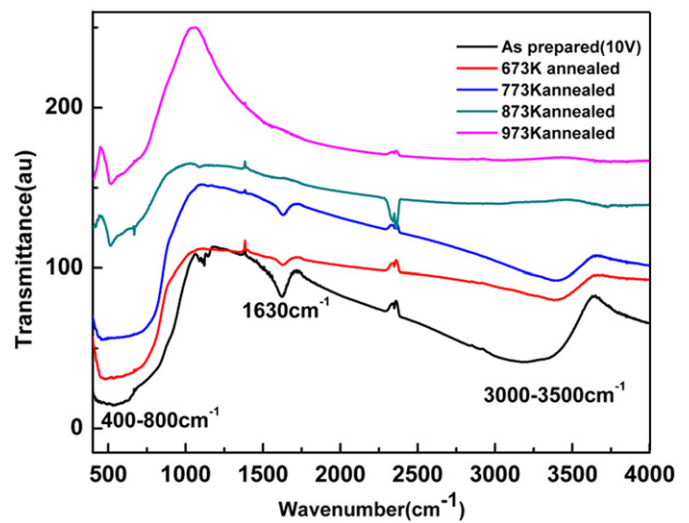


Fig. 16. FTIR spectra of the NP1 samples annealed at various temperatures.

nanotube powders. Such an exercise is currently underway in our studies.

3.9. Fourier transform infrared spectroscopic analysis

The FTIR spectra of the as prepared sample NP1 as well as the annealed NP1 samples are shown in Fig. 16. The spectra show strong absorption bands at 3200–3600 and 1630 cm^{-1} , for the as prepared samples, that are attributable to the stretching mode of the OH group and the deformation mode of the molecular water respectively. This characteristic mode reveals that there is chemisorbed as well as physisorbed hydroxyl species on the surface of TiO_2 nanotubes [48]. The same features were present in the IR spectra of the samples annealed at 673 and 773 K. However, in the case of samples annealed at 873 and 973 K the characteristic vibrational modes corresponding to the OH groups were absent. There is an additional broad band over the range of $400\text{--}800\text{ cm}^{-1}$ that corresponds to the characteristic peak of TiO_6 octahedra [49,50]. As the annealing temperature increases this band becomes sharper suggesting that the Ti-OH bonds converts to a strong network of Ti-O-Ti in TiO_2 skeleton. The present data obtained agrees well with the reported values [48,51]. From the FTIR studies of the nanotube powders it is clear that surface hydroxyl species are present which is important in the photo catalytic applications. Presence of surface hydroxyl groups creates an oxygen deficiency in TiO_2 matrix and results in the formation of Ti^{3+} , which are essential in photocatalysis [48]. It was shown by Wahlstrom et al. [52] that the presence of oxygen vacancies will enhance the decomposition of surface adsorbate (organic pollutants) by the process of increase in oxygen diffusion in the TiO_2 matrix. So combining anatase phase and surface hydroxyl group effect TiO_2 nanotube powders can be used effectively as photocatalysts for the decomposition of organic pollutants.

4. Conclusions

High aspect ratio anatase phase titania nanotube powders were synthesized by rapid breakdown anodization technique. The method is simple, cost effective and easy. The yield of the titania nanotube powders were high compared to other synthesis techniques. Even though potentiostatic anodization was employed, the transient was completely different from the expected one.

This may be attributed to the periodic release of the titania formed on surface. A change in the electrochemical conditions does not have much influence on the sample morphology. However, growth rate varied with the experimental conditions. The powders were confirmed to have tubular morphology with ~8 nm inner diameter and ~5 nm wall thickness by FESEM and TEM analysis. The SAED, XRD and Raman spectra revealed that these nanotubes are polycrystalline and is of anatase phase having crystallite size varying from 9 to 13 nm. Raman spectra revealed signature of optical phonon confinement and presence of non-zone center phonons. The morphology and phase changes of the samples annealed at different temperatures, as revealed by various techniques, enable in fixing the annealing temperature to confine to particular morphology and phase depending on the application. The photoluminescence of the nanotubes shows a temperature dependence that can be ascribed to the change in crystallinity and microstructure with annealing temperature. The as prepared samples showed good optical properties where the band gaps varied from 2.95 to 3.07 eV. FTIR, PL and DRS studies revealed the presence of defect states which is crucial for the photocatalytic applications. Comparing with the titania nanotube arrays, even though self-organized property of the material were lost in the present case, the nanotubes are of smaller diameter and wall thickness, and exhibited quantum confinement. When the titania nanotube arrays are amorphous in the as prepared condition, the nanotube powders are of anatase phase. The as prepared TiO_2 nanotubes can be spray coated, spin coated, dip coated or screen printed on different substrates such as quartz, silicon and FTO/ITO coated glasses for device applications.

Acknowledgments

Authors acknowledge Institute of Nano-science Initiative (INI), IISc, Bangalore for the FESEM analysis, Dr. M.T. Jose, Radiological Safety Division, IGCAR for the photoluminescence studies and Dr. S. Kalavathi, Material Science Group, IGCAR for X-ray diffraction Studies.

References

- [1] M. Paulose, G.K. Mor, O.K. Varghese, K. Shankar, C. Grimes, *J. Photochem. Photobiol. A* 178 (2006) 8–15.
- [2] S.C. Roy, O.K. Varghese, M. Paulose, C.A. Grimes, *ACS Nano* 4 (2010) 1259–1278.
- [3] I.P. Parkin, R.G. Palgrave, *J. Mater. Chem.* 15 (2005) 1689–1695.
- [4] J.R. Jennings, A. Ghicov, L.M. Peter, P. Schmuki, A.B. Walker, *J. Am. Chem. Soc.* 130 (2008) 13364–13372.
- [5] G.K. Mor, O.K. Varghese, M. Paulose, K.G. Ong, C.A. Grimes, *Thin Solid Films* 496 (2006) 42–48.
- [6] S. Eun, J. Hoon, S. Cheon, S. Nam, H. Kangand, J. Choi, *Electrochim. Acta* 53 (2008) 4846–4851.
- [7] K.S. Raja, M. Misra, V.K. Mahajan, T. Gandhi, P. Pillai, S.K. Mohapatra, *J. Power Sources* 161 (2006) 1450–1457.
- [8] C. Su, B. Hong, C. Tseng, *Catal. Today* 96 (2004) 119–126.
- [9] H. Hayashi, K. Torii, *J. Mater. Chem.* 12 (2002) 3671–3676.
- [10] S.I. Matsushita, T. Miwa, D.A. Tryk, A. Fujishima, *Langmuir* 14 (1998) 6441–6447.
- [11] V. Zwilling, D. David, M.Y. Perrin, M. Aucouturier, *Surf. Interface Anal.* 637 (1999) 629–637.
- [12] R. Beranek, H. Hildebr, P. Schmuki, *Electrochim. Solid-State Lett.* 6 (B12–B14) (2003) 14–16.
- [13] Q. Cai, M. Paulose, O.K. Varghese, C.A. Grimes, *J. Mater. Res.* 20 (2005) 230–236.
- [14] J. Wang, Z. Lin, *Chem. Mater.* 20 (2008) 1257–1261.
- [15] J.M. Macak, M. Zlamal, J. Krysa, P. Schmuki, *Small* 3 (2007) 300–304.
- [16] J.M. Macak, H. Tsuchiya, P. Schmuki, *Angew. Chem. Int. Ed.* 44 (2005) 2100–2102.
- [17] M. Paulose, H.E. Prakasam, O.K. Varghese, L. Peng, K.C. Popat, G.K. Mor, *J. Phys. Chem. C* 111 (2007) 14992–14997.
- [18] J.M. Macak, P. Schmuki, *Electrochim. Acta* 52 (2006) 1258–1264.
- [19] M. Paulose, K. Shankar, S. Yoriya, H.E. Prakasam, O.K. Varghese, G.K. Mor, *J. Phys. Chem. B* 110 (2006) 16179–16184.
- [20] J.M. Macak, H. Tsuchiya, A. Ghicov, K. Yasuda, R. Hahn, S. Bauer, *Curr. Opin. Solid State Mater. Sci.* 11 (2007) 3–18.
- [21] H.E. Prakasam, K. Shankar, M. Paulose, O.K. Varghese, C.A. Grimes, *J. Phys. Chem. C* 111 (2007) 7235–7241.
- [22] R. Narayanan, T.Y. Kwon, K.H. Kim, *Mater. Lett.* 63 (2009) 2003–2006.
- [23] V. Vega, M.A. Cerdeira, V.M. Prida, D. Alberts, N. Bordel, R. Pereiro, F. Mera, S. Garcia, M. Hernandez-Velez, M. Vazquez, *J. Non-Cryst. Solids* 354 (2008) 5233–5235.
- [24] C.C. Wen, C.S. Hsieh, E.W. Diau, *Appl. Phys.* 95 (2009) 889–898.
- [25] L.V. Taveira, J.M. Macak, H. Tsuchiya, L.F. Dick, P. Schmuki, *J. Electrochem. Soc.* 152 (2005) B405–B410.
- [26] Y. Tang, J. Tao, Y. Zhang, T. Wu, H. Tao, Y. Zhu, *Trans. Nonferrous Met. Soc. China* 19 (2008) 192–198.
- [27] G.K. Mor, H.E. Prakasam, O.K. Varghese, K. Shankar, C.A. Grimes, G.K. Mor, *Nano Lett.* 7 (2007) 2356–2364.
- [28] J.M. Macak, H. Tsuchiya, S. Berger, S. Bauer, S. Fujimoto, P. Schmuki, *Chem. Phys. Lett.* 428 (2006) 421–425.
- [29] O.K. Varghese, M. Paulose, C.A. Grimes, *Nat. Nanotechnol.* 4 (2009) 592–597.
- [30] R. Hahn, J.M. Macak, P. Schmuki, *Electrochim. Commun.* 9 (2007) 947–952.
- [31] Q.A. Nguyen, Y.V. Bhargava, T.M. Devine, *Electrochim. Commun.* 10 (2008) 471–475.
- [32] N.F. Fahim, M.F. Mork, T. Sekino, *Electrochim. Acta* 54 (2009) 3255–3269.
- [33] B.C. Richter, Z. Wu, E. Panaiteescu, R.J. Willey, L. Menon, *Adv. Mater.* 19 (2007) 946–948.
- [34] N.K. Allam, C.A. Grimes, *J. Phys. Chem. C* 111 (2007) 13028–13032.
- [35] N.F. Fahim, T. Sekino, *Chem. Mater.* 21 (2009) 1967–1979.
- [36] P. Scherrer, *Gottinger Nachrichten*, vol. 2, 1918, p. 98.
- [37] M.Z. Hu, P. Lai, M.S. Bhuiya, C. Tsouris, B. Gu, M. Paranthaman, J. Gabitto, L. Harrison, *J. Mater. Sci.* 44 (2009) 2820–2827.
- [38] C.Y. Xu, P.X. Zhang, L. Yan, *J. Raman Spectrosc.* 32 (2001) 862–865.
- [39] A. Pottier, S. Cassaignon, C. Chaneac, F. Villain, E. Tronc, J.P. Jolivet, *J. Mater. Chem.* 13 (2003) 877–882.
- [40] X.Z. Li, F.B. Li, C.L. Yang, W.K. Ge, *J. Photochem. Photobiol.-A* 141 (2001) 209–217.
- [41] G.A. Martinez Castanon, M.G. Sanchez Loredo, H.J. Dorantes, J.R. Martinez Mendez, G. Ortega-Zarzosa, F. Riuz, *Mater. Lett.* 59 (2005) 529–534.
- [42] M. Nowak, P. Spzperlich, L. Bober, J. Szala, G. Moskal, D. Stroz, *Ultrasound Sonochem.* 15 (2008) 709–716.
- [43] W. Macyk, G. Burgeth, H. Kisch, *Photochem. Photobiol. Sci.* 2 (2003) 322–328.
- [44] J. Tauc, *Mater. Res. Bull.* 5 (1970) 721–730.
- [45] R. Asahi, T. Morikawa, T. Ohwaki, K. Aoki, Y. Taga, *Science* 293 (2001) 269–271.
- [46] K.M. Reddy, B. Baruwati, M. Jayalakshmi, M.M. Rao, *J. Solid State Chem.* 178 (2005) 3352–3358.
- [47] N. Tio, K. Lv, H. Zuo, J. Sun, K. Deng, S. Liu, *J. Hazard. Mater.* 161 (2009) 396–401.
- [48] H. Jensen, A. Soloviev, Z. Li, E.G. Sogaard, *Appl. Surf. Sci.* 246 (2005) 239.
- [49] V.A. Zeitler, C.A. Brown, *J. Phys. Chem.* 61 (1957) 1174.
- [50] K.A. Mautitz, C.K. Jones, *J. Appl. Polym. Sci.* 40 (1990) 1401.
- [51] S. Madhu Kumar, Badrinarayanan, M. Sastry, *Thin Solid Films* 358 (2000) 122.
- [52] E. Wahlstrom, E.K. Vestergaard, R. Schaub, A. Ronna, M. Vestergaard, E. Laegsgaard, I. Stensgaard, F. Besenbacher, *Science* 303 (2004) 511.